Acta Materialia 238 (2022) 118187

Contents lists available at ScienceDirect

Acta Materialia

journal homepage: www.elsevier.com/locate/actamat

Microstructure and mechanical properties of 3D ink-extruded CoCrCuFeNi microlattices

Dingchang Zhang, Christoph Kenel, David C. Dunand*

Department of Materials Science and Engineering, McCormick School of Engineering, Northwestern University, 2220 Campus Drive, Evanston, IL 60208, USA

ARTICLE INFO

Article history:
Received 24 March 2022
Revised 17 June 2022
Accepted 16 July 2022
Available online 17 July 2022

Keywords:
Additive manufacturing
High-energy X-ray diffraction
Reduction
Metal foam
Finite element modeling

ABSTRACT

Microlattices with orthogonal 0-90° architecture are 3D-extrusion printed from inks containing a blend of oxide powders (Co_3O_4, CuO, Fe_2O_3, and NiO) and metal powder (Cr). Equiatomic CoCrCuFeNi microlattices with ~170 μm diameter struts are then synthesized by H_2-reduction of the oxides followed by sintering and interdiffusion of the resulting metals. These process steps are studied by *in-situ* synchrotron X-ray diffraction on single extruded microfilaments (lattice struts) with ~250 μm diameter. After reduction and partial interdiffusion at 600 °C for 1 h under H_2, filaments consist of lightly-sintered metallic particles with some unreduced Cr_2O_3. A reduced, nearly fully densified (porosity: 1.6 ± 0.7%) alloy is obtained after solid-state homogenization at 1050 °C for 4 h under H_2, with a microstructure consisting of two face-centered-cubic phases, one Cu-poor and the other Cu-rich. When a 10 min excursion to 1150 °C is added to the 1050 °C homogenization, a Cu-rich melt forms which enhances densification (porosity: 0.3 ± 0.2%) and smooths both strut surfaces and sharp cusps at nodes in the microlattices. The liquid-sintered microlattices show higher compressive strength and ductility than the solid-sintered microlattices. These improvements are consistent with finite-element modeling results which show that smoothening of the sharp cusps at nodes by the solidified melt reduces stress concentrations. These CoCrCuFeNi microlattices can be integrated in more complex load-bearing applications, e.g., as cores of sandwich structures with an unusual combination of high specific stiffness, strength, and toughness.

© 2022 Acta Materialia Inc. Published by Elsevier Ltd. All rights reserved.

1. Introduction

High-entropy alloys (HEAs) are a group of alloys that mix five or more principal elements, with each element having a concentration between 5 and 35 at.% [1,2]. The ductile, equiatomic CoCrFeNi ($Co_{25}Cr_{25}Fe_{25}Ni_{25}$) alloy can be further alloyed with Al, Mn, Ti, or Cu to obtain various HEA variants with a range of properties such as strength, fracture toughness, and corrosion resistance. [3–5]. Among CoCrFeNi-based quinary HEAs, equiatomic CoCrCuFeNi ($Co_{20}Cr_{20}Cu_{20}Fe_{20}Ni_{20}$) has been widely studied in recent years [6–9]. Copper in this HEA provides antibacterial ability superior to those of traditional Cu-bearing stainless steel, making CoCrCuFeNi useful for applications such as biomedical instruments, food industry, and marine equipment, preventing microbiologically influenced corrosion [10–12]. Also, high-temperature wear resistance is better for CoCrCuFeNi than for CoCrFeNi due to the self-lubricating properties of Cu at 600 °C [13]. Finally, CoCrCuFeNi is suitable for semi-solid processing, as it shows thixotropic behavior in its solidus-liquidus temperature range [14].

Additive manufacturing (AM) of HEAs can efficiently produce complex shapes at lower feedstock consumption [15]. Most studies use Direct Laser Deposition (DLD), Laser Powder Bed Fusion (L-PBF), or Electron Beam Melting (EBM) to fabricate high-entropy alloy specimens, where a laser or electron beam is used to melt a powder stream or a powder bed, layer by layer [16]. Two common features of these processes are: (i) the very high cooling rates during the solidification of the melt pool and (ii) the cyclic thermal input when new layers are melted on top of already solidified ones. These processes refine grain size and suppress elemental segregation, which improves strength and helps to form a single solid solution [11,17,18]. For example, $Fe_{40}Mn_{20}Co_{20}Cr_{15}Si_5$ fabricated by L-PBF has higher strength and ductility than cast samples because of its finer grains, higher dislocation density, and improved twinning capability from more metastable phases [19]. However, textured microstructures, columnar grains, and large residual stresses are usually formed during AM of HEAs, potentially resulting in anisotropic mechanical behavior, distortion or cracking of printed parts, and lower fatigue life [20–22]. For example, $AlCoCrFeNi_{2.1}$ ($Al_{16.4}Co_{16.4}Cr_{16.4}Fe_{16.4}Ni_{34.5}$) fabricated by DLD shows higher strength in deposition direction than in scanning direction due to different fractions of dendritic and eutectic phases in these two directions [21].

* Corresponding author.
E-mail address: dunand@northwestern.edu (D.C. Dunand).

https://doi.org/10.1016/j.actamat.2022.118187
1359-6454/© 2022 Acta Materialia Inc. Published by Elsevier Ltd. All rights reserved.

3D ink-extrusion printing is an alternative AM method where a powder-loaded ink is extruded layer by layer, in air, and at ambient temperature; the printed green part is then debinded and sintered to achieve full densification [23]. CoCrFeNi microlattices fabricated by this method show a uniform single-phase microstructure without warpage or cracking due to minimal thermal stresses during isothermal sintering [24]. 3D ink-extrusion printing uses elemental or pre-alloyed metal powder to form alloys via interdiffusion and sintering. Alternatively, metal compounds (such as metal oxide, hydrides, or salts) can be used, which, after reduction (using H_2 or CO) or vacuum decomposition (for hydrides), form in situ metal powders [23–29]. These precursor powders can have a sub-micron to nanometer size with irregular morphology [30–33], unlike powder-bed-based AM methods which require powders with large sizes and spherical shapes to insure good flowability [34,35]. Recently, we fabricated quaternary equiatomic CoCrFeNi microlattices by ink-printing powder blend of Co_3O_4 + Cr_2O_3 + Fe_2O_3 + NiO; after reduction, interdiffusion, and sintering under hydrogen, the microlattices were nearly pore-free, chemically homogenous and mechanically strong and ductile [24]. Peng et al. also recently produced CoCrFeNiMn HEA microlattices by ink-printing of pre-alloyed powder, followed by sintering. The resulting HEA microlattices demonstrated a high strain hardening and energy absorption [36]. We are not aware of any other HEAs in the literature which were 3D ink-extrusion printed.

Here, we study quinary, equiatomic CoCrCuFeNi HEA lattices fabricated by 3D ink-extrusion printing of inks containing a blend of Co_3O_4, CuO, Fe_2O_3, NiO, and Cr_2O_3 (or Cr) powders. Comparing micron-size oxide and metallic powders, the former exhibit much lower cost without pyrophoric risks. Once reduced, the micron size of the metal powders enables rapid sintering and homogenization, due to high surface area and short diffusion distances, respectively. *In situ* synchrotron X-ray diffraction is used to follow the sequential reduction and metallic phase evolution of an all-oxide blend heated under pure hydrogen. Microstructural evolution is studied for blends containing pure Cr based on the *in situ* XRD study showing sluggish reduction of Cr_2O_3. A dual-phase face-centered cubic (fcc) CoCrCuFeNi HEA is obtained with two distinctly different microstructures after solid-phase and liquid-phase sintering, respectively. The mechanical properties of these CoCrCuFeNi lattices with these two micro- and macro-structures are measured in compression and compared to finite element modeling predictions.

2. Experimental Procedures

2.1. Alloy synthesis and extrusion printing

Inks for 3D printing are prepared by mixing Fe_2O_3 (total weight in mixture: 2.04 g, purity: ≥99%, powder size: <5 µm, supplier: Sigma Aldrich), NiO (1.91 g, 99%, <44 µm, Sigma Aldrich), Co_3O_4 (2.06 g, <10 µm, Sigma Aldrich), Cr (1.33 g, 99.5%, 3 µm, US Research Nanomaterials), CuO (2.04 g, 99.5%, 0.5 µm, US Research Nanomaterials) powders, poly-lactic-co-glycolic-acid (0.87g, PLGA, Evonik Industries) as binder, dibutyl phthalate (1.58g, DBP, Sigma-Aldrich) as plasticizer, ethylene glycol butyl ether (0.79g, EGBE, Sigma-Aldrich) as surfactant into dichloromethane (20 ml, DCM, Sigma-Aldrich) as solvent. For the in-situ X-ray diffraction experiments, Cr_2O_3 (3.89 g, 99.7%, <44 µm, Alfa Aesar) rather than Cr powders were used in the extruded specimens. The micrometric size of the powders is essential for their printability and their rapid densification and homogenization during sintering. Fine oxide powders can be obtained at a lower cost than pure metal powders of the same size due to their lack of reactivity with air. Wet milling is firstly carried out in a steel milling vial for 30 min to mix powders with 8 ml DCM and EGBE. Then, the milling process is performed for another 5 min after adding 12 ml DCM, PLGA (dissolved), and DBP. The viscosity of the inks is adjusted by DCM evaporation at 50 °C to get a printable ink (the rheological properties of the PLGA-DBP-DCM ink system have been studied in detail in Ref. [23]). Extrusion printing is performed with a 3D-Bioplotter (EnvisionTEC, Germany) with conical 250 µm plastic nozzles (Nordson EFD). The 5 × 5 × 10 mm^3 lattices are printed with a layer height of 200 µm, a horizontal spacing of 0.5 mm, and a layer rotation angle of 90°. Printing parameters for lattices are chosen based on previous studies on CoCrFeNi microlattices [24].

The printed filaments and microlattices are sintered under flowing hydrogen (99.999% pure) in a half-covered alumina boat in which a pure copper piece was also placed to prevent Cu losses by creating a Cu partial pressure. Three steps are included in the de-binding and sintering process: (i) evaporation of residual DCM solvent and EGBE at 150 °C for 30 min; (ii) decomposition of PLGA binder polymer at 300 °C for 30 min, and (iii) sintering at the final temperature. The heating and cooling rates are 10 °C/ min. One of three final temperatures is used: (i) 1050 °C for 4 h, (ii) 1100 °C for 4 h, or (iii) 1050-1150 °C for 4 h, consisting of two plateaus at 1050 °C, each lasting for 105 min interspersed by a 30 min excursion to 1150 °C (10 min ramping up from 1050 °C, 10 min hold at 1150 °C and 10 min ramping down to 1050 °C).

2.2. In situ X-ray diffraction

In situ X-ray diffraction is performed using a setup deployed at the Material Science powder diffraction beamline X04SA of the Swiss Light Source (Paul Scherrer Institut, Switzerland) as described in detail in Ref. [24]. In brief, the measurement is performed with a monochromatic beam (19.9 keV, 0.7 × 1.4 mm) on a single, ink-printed Co_3O_4-Cr_2O_3-Fe_2O_3-NiO-CuO microfilament (target composition: equiatomic CoCrCuFeNi; size: ~2 × 0.25 × 0.25 mm^3) lodged in an externally-heated quartz capillary (0.5 mm OD) flushed with a continuous flow (1.3 ml/min) of 99.9999% pure H_2. Diffraction spectra are detected on a Mythen II array with 120° 2θ coverage, 24 s exposure, and 3° specimen rocking angle. For calibration, LaB_6 (NIST 660c) and Si (NIST 640c) powders are used. Data post-processing and plotting are performed using Python (Anaconda, Continuum Analytics). Perceptually-uniform color maps are retrieved from the cmocean package [37]. All diffractograms are background-corrected using asymmetric least-squares smoothing [38]. Integrated peak areas are calculated by direct numerical integration of the measured data.

2.3. Characterization

Metallographic characterizations are done on polished cross-sections of filaments and lattices. Samples are cold mounted in epoxy resin, ground with SiC grinding papers, polished with diamond suspensions (3 and 1 µm) and colloidal silica (0.02 µm), and coated with 8 nm Os. Scanning electron microscopy (SEM) is performed on a JEOL JSM-7900FLV instrument equipped with an Oxford Ultimax EDS detector. EBSD is performed on a Quanta 650 instrument with an Oxford Symmetry 2 detector. Surface roughness measurements were carried out on an Olympus 3D Laser Confocal Microscope with MPLAPON50xLEXT objective. The threshold between roughness and waviness components is set at 100 µm.

Thermogravimetric analysis (TGA) is carried out on Mettler Toledo TGA/DSC 3+. The filaments containing blended Co_3O_4-Cr-Fe_2O_3-NiO-CuO particles are first reduced at 1000 °C for 1 h under pure H_2. Then, TGA is performed under Ar/4% H_2 cover gas, with the filaments in an alumina crucible being heated and cooled three times between 900 and 1200 °C, with a heating/cooling rate of 10 °C/ min.

Vickers microhardness is measured on a Wilson VH3100 Automated Micro-hardness Tester by applying 1.96 N for 10 s for at

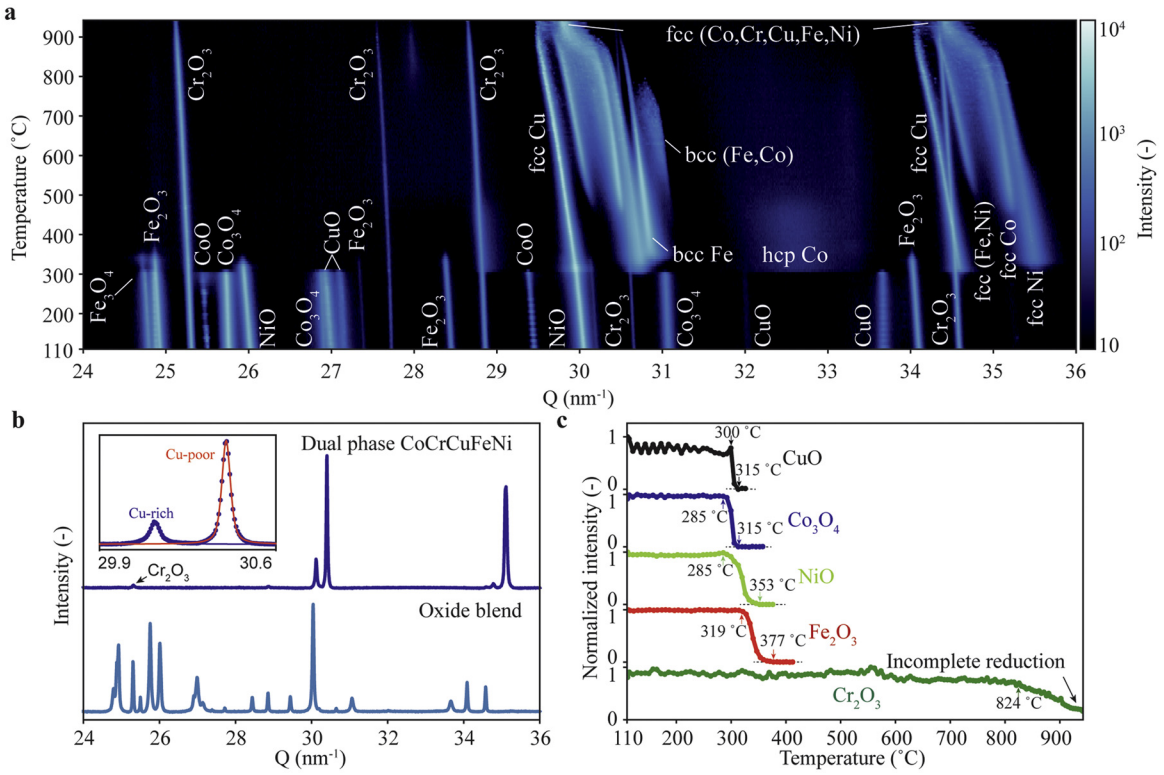

Fig. 1. (a) Stacked X-ray spectra acquired during *in-situ* diffraction of a microfilament extruded from a blended Co_3O_4-Cr_2O_3-Fe_2O_3-NiO-CuO ink, upon heating in H_2 from 110 to 943 °C. (b) XRD diffractogram before and after reduction in H_2 showing the formation of a dual-phase fcc HEA with residual Cr_2O_3. (c) Normalized diffraction peak intensity for CuO, Co_3O_4, NiO, Fe_2O_3, and Cr_2O_3 oxides as a function of temperature upon H_2 reduction, showing temperatures for onset and end of reduction.

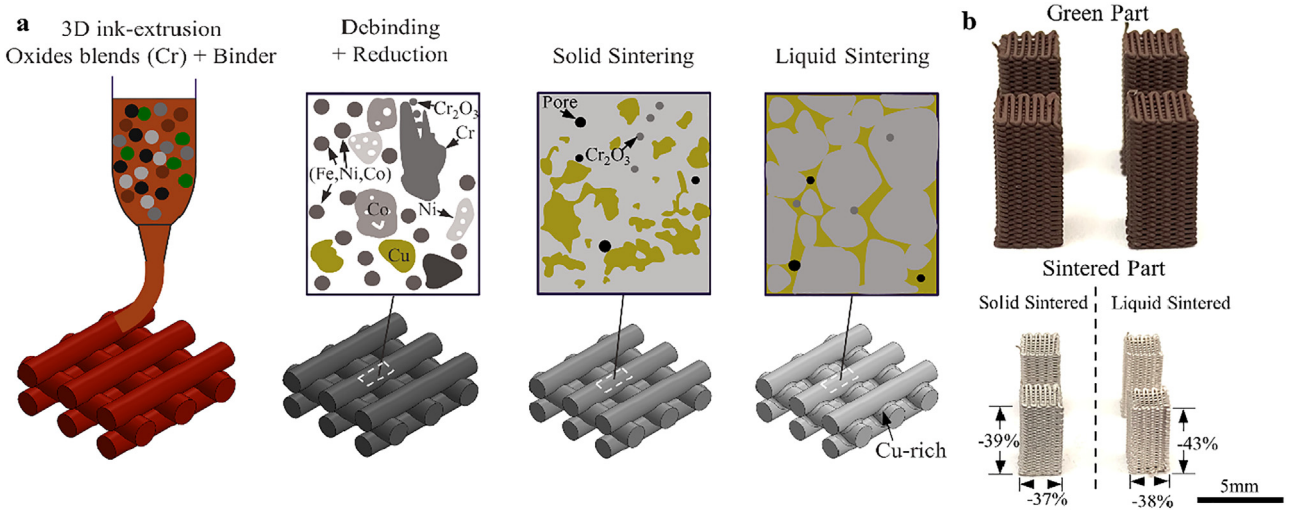

Fig. 2. (a) Schematic of 3D ink extrusion, reduction, and sintering process; (b) photographs of CoCrCuFeNi microlattices printed from Co_3O_4-Cr-Fe_2O_3-NiO-CuO inks, (left) after solid sintering (1050 °C / 4 h) and (right) after liquid sintering (1050-1150 °C / 4 h).

least ten points. Compression tests are carried out at room temperature with an initial strain rate of $5 \times 10^{-4}\,s^{-1}$ on a Sintech 20 G (MTS, USA) with a 100 kN load cell, using oil-lubricated platens. To ensure uniaxial compression, the top and bottom surfaces of sintered lattices are ground parallel before the compression test.

3. Results and Discussion

3.1. In situ X-Ray Diffraction

The reduction in H_2 and phase evolution are shown as a function of temperature in Fig. 1, for a microfilament 3D-extruded from inks containing blended Co_3O_4, Cr_2O_3, CuO, Fe_2O_3, and NiO oxides (target: equiatomic CoCrCuFeNi) studied by in-situ X-ray diffraction. The start and end temperatures of reduction for CuO, Co_3O_4, NiO, and Fe_2O_3 are labeled in Fig. 1(c). Three oxides start reducing in a narrow range of temperature: at 285 °C for Co_3O_4 and NiO, and at 300 °C for CuO. At a somewhat higher temperature of 319 °C, Fe_2O_3 then starts reduction. Reduction is completed at 315 °C for Co_3O_4 and CuO, at 353 °C for NiO and at 377 °C for Fe_2O_3. The temperature ranges between start and end of reduction increase from CuO (15 °C), to Co_3O_4 (30 °C) to Fe_2O_3 (58 °C) and finally to NiO (68 °C). Above 377 °C, metallic Co, Ni, Fe, and Cu coexist with Cr_2O_3 which starts to significantly reduce at a much higher temperature (~824°C). Cr_2O_3 particle reduction is facilitated by a surrounding metallic matrix with high Cr solubility,

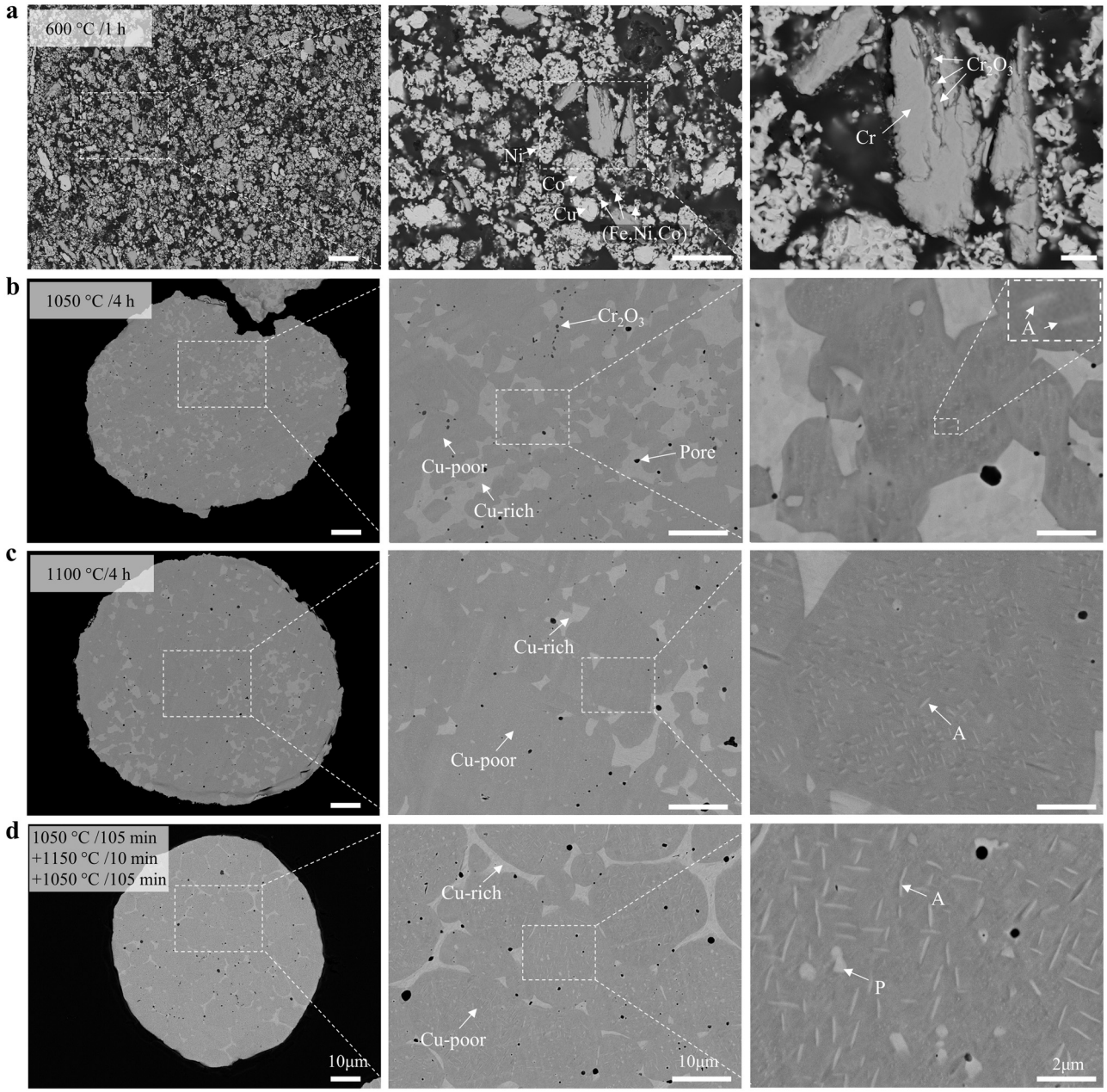

Fig. 3. SEM-BSE micrographs of strut cross-sections in 3D ink-extrusion printed and co-reduced lattices. The struts were extruded from Co_3O_4-Cr-Fe_2O_3-NiO-CuO inks and were heated in H_2 at (a) 600 °C for 1 h, (b) 1050 °C for 4 h, (c) 1100 °C for 4 h (solid-state sintering) and (d) 1050 + 1150 °C for 4 h (liquid-phase sintering). A/P: acicular/plate-like Cu-rich phase, probably the same phase oriented at different angles with respect to the cross-section.

which removes reduced Cr from the reduction site by diffusion, protecting it from re-oxidation and reducing the energy barrier to form metallic Cr nuclei [39,40]. After reduction, metallic Co, Ni, Fe, and Cu interdiffuse. At first, solid-solution bcc (Fe, Co) and fcc (Fe, Ni) are formed by interdiffusion of nascent Co, Fe, and Ni. Subsequently, Co, Fe, Ni, (Fe,Ni), (Fe,Co) and locally reduced Cr all interdiffuse to form a high-entropy fcc phase, which is Cu-poor, similar to the one observed in a previous study on a CoCrFeNi alloy [24]. Also, a Cu-rich phase appears upon onset of CuO reduction (~300 °C) and remains until the end of the experiment. Only in the last stages of the heating ramp, between 900 and 943 °C, do the diffraction peak positions start to deviate from pure thermal expansion and shift slightly towards larger Q, or smaller lattice parameters, indicating minor alloying of the Cu-rich phase. After cooling, the dual-phase fcc structure is confirmed, comprising a Cu-rich phase with a larger lattice parameter (3.6124 Å), and a Cu-poor phase with a smaller one (3.5798 Å), as shown in Supplementary Figure 1. These values are close the reported lattice parameters in a CoCrCuFeNi alloy thixo-formed at 1150 ℃ [14]: 3.609 Å for the Cu-rich phase (with 83.2 at.% Cu, as measured via energy-dispersive X-ray spectroscopy in electron-transparent foils) and 3.584 Å for the Cu-poor phase (with 9.5 at.% Cu). XRD of our specimen also reveals that residual Cr_2O_3 remains in the structure (Fig. 1b and c), likely caused by sintering of the metallic phases, facilitated by rapidly diffusing Cu at its high homologous temperature. This sintering traps Cr_2O_3 in the matrix with no access to reducing H_2 nor the ability to remove the formed H_2O.

3.2. 3D-printing and sintering

3.2.1. 3D ink-extrusion printed lattices

First, experiments are conducted on microfilaments extruded from Co_3O_4-Cr_2O_3-Fe_2O_3-NiO-CuO inks which were reduced and sintered at four temperatures (1000, 1100, 1200, or 1300 °C) under

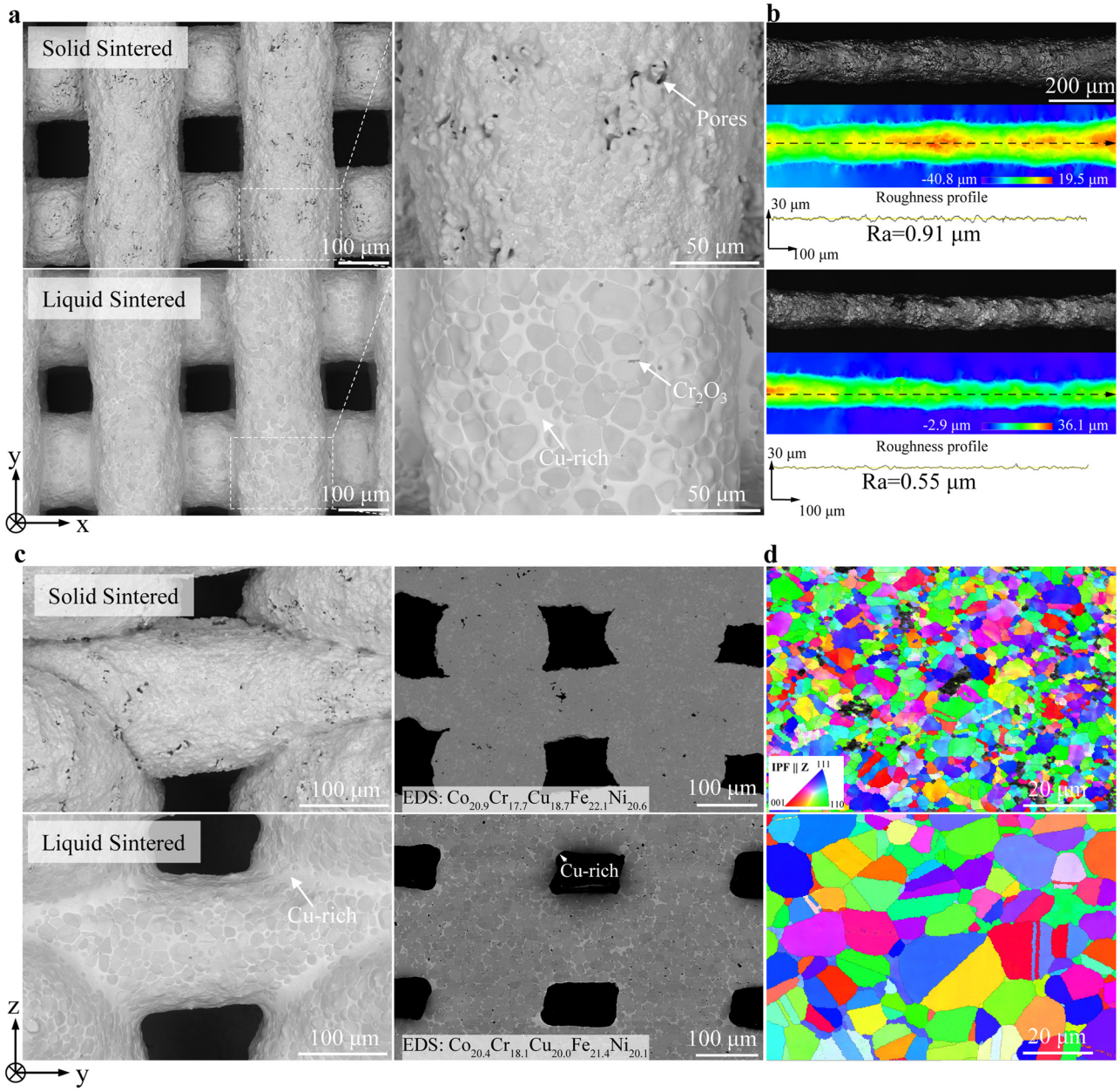

Fig. 4. Micrographs of 3D ink-extrusion printed, co-reduced, and sintered lattices for (a) top view from SEM-BSE, (b) roughness profile after subtracting waviness component on filaments from laser confocal microscope, (c) side view and cross-sections from SEM-BSE and (d) inverse pole figure (IPF) map from EBSD. The lattices printed from blended Co_3O_4-Cr-Fe_2O_3-NiO-CuO powders are sintered in H_2: (top row) at 1050 °C for 4 h under solid sintering and (bottom row) at 1050 + 1150 °C for 4 h under liquid sintering. The chemical compositions from EDS are shown in (c).

pure H_2 (Supplementary Figure 2). They showed that Cr_2O_3 is fully reduced only at the highest temperature of 1300 °C. However, increasing the temperature to 1300°C to fully reduce the Cr_2O_3 leads to excessive Cu evaporation from the liquid Cu-rich phase, given the high vapor pressure of Cu at that temperature (Supplementary Figure 2). Based on the above in situ XRD and sintering experiments, pure elemental Cr powder rather than Cr_2O_3 is used in powder blends for the 3D printing study, to exclude effects from unreduced, encapsulated Cr_2O_3. Compared with single-phase CoCrFeNi, our dual-phase CoCrCuFeNi alloy forms a Cu-rich liquid phase during sintering, with a large difference between solidus and liquidus in this alloy. The low solidus temperature is critical for the sintering process, as the excessive formation of the liquid phase can induce slumping under gravity, which can destroy the 3D printed structure. However, it also allows liquid phase sintering or thixo-casting [14]. Based on the thermogravimetric analysis (shown in Supplementary Figure 3), the solidus temperature of the co-reduced CoCrCuFeNi HEA is 1112 °C, which is 29 °C higher than the melting point of pure Cu (1083 °C). As shown in Supplementary Figure 4, the Cu-rich phase has a composition Cu-3Co-1Cr-3Fe-7Ni and Cu-3Co-2Cr-2Fe-7Ni (at.%), as measured by EDS on two samples. The presence of Co, Fe and Ni are expected to increase the solidus temperature of the Cu-rich phase, given that the Cu-X (X=Co,Fe,Cr) binary alloy systems have peritectic or eutectic temperatures of 1113 °C (Cu-Co) [41], 1088 °C (Cu-Fe) [42] and 1077 °C (Cu-Cr) [43], and that the Cu-Ni alloy system shows a near-linear increase of solidus temperature from 1083 (for pure Cu) to 1455 °C (for pure Ni) [44]. Based on the measured 1112 °C solidus temperature of our CoCrCuFeNi HEA, two sintering treatments were chosen: (i) fully below the solidus temperature (4 h

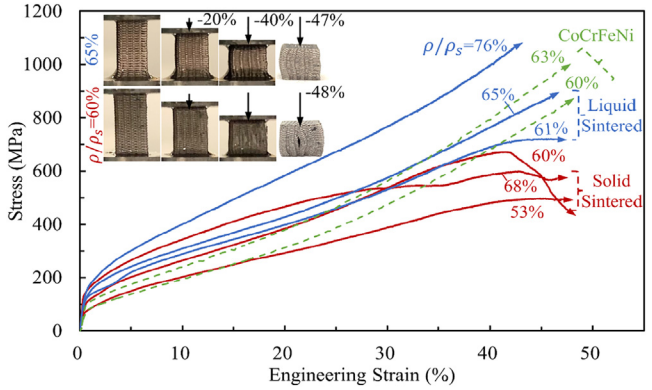

Fig. 5. Compressive stress-strain curves for HEA lattices made from CoCrFeNiCu (present study) and CoCrFeNi (from Ref. [24], up to 50% strain). The insets show side views of CoCrFeNiCu lattices with relative density ρ/ρ_s = 60% (solid-sintered) and ρ/ρ_s = 65% (liquid-sintered) before and after 20, 40 and 47/48% deformation.

at 1050 °C) and (ii) partially above the solidus temperature (4 h at 1050 / 1150 °C).

Microlattices were 3D-printed from Co_3O_4-Cr-Fe_2O_3-NiO-CuO inks, reduced, and sintered into dense, equiatomic CoCrFeNiCu HEA, as schematically shown in Fig. 2(a). Photographs of green and sintered lattices are shown in Fig. 2(b). The green oxide lattices show significant shrinkage after sintering due to the removal of binder, oxygen from oxides, and pores. Shrinkage is somewhat higher in the vertical direction (39-43%) than in the horizontal direction (37-38%), possibly because of the effect of gravity. Nevertheless, warpage is not observed. The liquid-state sintered lattices show higher shrinkage, consistent with more complete elimination of residual pores as compared to solid-state sintering.

3.2.2. Microstructural evolution after reduction and sintering

Fig. 3 shows the microstructural evolution after reduction and sintering of single cylindrical struts cut from lattices. In the as-printed struts, the loosely packed oxide particles are held together by the PLGA binder polymer. After debinding at 300 °C and reduction at 600 °C, an arrangement of loosely packed metal particles is observed (Fig. 3(a)). Co_3O_4, CuO, and NiO powders are reduced to Co, Cu, and Ni particles, respectively, as determined via SEM-EDS. Fe_2O_3 powders are reduced to Fe particles, which already contain a substantial amount of Ni and Co in solid solution, due to inter-diffusion during heating. This agrees with the *in situ* XRD study showing the early formation of (Fe,Ni) and (Fe,Co) solid solutions (Fig. 1). The Cr powders remain predominantly metallic except for rare micron-size Cr_2O_3 particles formed along cracks, possibly because of H_2O vapor released during reduction of the surrounding oxides (Fig. 3(a)). Similar to adding Cr_2O_3 in the powder blend, these Cr_2O_3 particles can then be encapsulated within the metallic matrix, losing access to hydrogen during sintering. After sintering at 1050 and 1100 °C for 4 h (Fig.s 3(b) and (c)), the struts are near-fully densified (porosity for (b): 1.7 ± 0.7%), with rare residual Cr_2O_3 particles and pores. The bright-gray phase is the Cu-rich, lower-melting phase, and the granular dark-gray is the Cu-poor, higher-melting phase, with $Co_3Cr_2Cu_{86}Fe_2Ni_7$ and $Co_{23}Cr_{20}Cu_{10}Fe_{24}Ni_{22}$ compositions for (d), respectively (Supplementary Figure 4). Similar phases were reported in Ref. [14], where thixo-formed CoCrCuFeNi HEA consists of $Co_3Cr_2Cu_{83}Fe_4Ni_8$ (Cu-rich) and $Co_{23}Cr_{24}Cu_{10}Fe_{22}Ni_{21}$ (Cu-poor) phases. A metastable single fcc phase was found in equiatomic CoCrCuFeNi HEA fabricated by SLM [11] and mechanical alloying [8,45], which forms due to the very high cooling rates during these processes. The mechanically-alloyed single fcc phase separated into two fcc phases when it was heated above 800 °C [45].

Within the Cu-poor phase, some bright-gray, acicular Cu-rich precipitates can be found (Fig. 3(c)), expected to have formed from Cu precipitating during cooling after sintering, and consistent with the positive mixing enthalpy of Cu with Co, Cr, Fe, and Ni which leads to phase separation and precipitation during cooling [46]. Zheng et al. proposed that the high diffusion coefficient of Cu also facilitates the segregation of a Cu-rich phase [47]. Coarsening of Cu-rich precipitates is observed for microstructure sintered at 1100 °C for 4 h (Fig. 3(d)). After liquid sintering (10 min above the 1112 °C solidus temperature, where the Cu-rich phase melts), the previously angular Cu-poor phase becomes smoother, and the Cu-rich phase, which appears to have wetted the Cu-poor phase when it was liquid, forms a continuous matrix after solidification. Liquid formation enables rapid dissolution and reprecipitation, and it thus accelerates compositional homogenization, facilitates removal of pores, and alters size and shape of Cu-poor solid phase, which shows a more rounded shape and a coarser size than in the solid-sintered samples. A similar microstructure was found in CoCrCuFeNi HEA thixo-cast at 1150 °C, where globular Cu-poor grains were surrounded by a continuous, lower-melting, Cu-rich phase [14].

Many alloys processed via additive manufacturing suffer from poor surface quality (arithmetic mean deviation Ra=17.9 ± 2 μm for L-PBF Ti-6Al-4V [48]), which often needs to be improved by post-treatments [49]. The surfaces of the struts of our micro-lattice are shown in Fig. 4. Low-magnification micrographs for these lattices are shown in Supplementary Figure 5. The solid- and liquid-sintered struts have a diameter of 176 ± 5 μm and 166 ± 4 μm, respectively. The porosity of solid sintered and liquid samples is 1.6 ± 0.7 and 0.3 ± 0.2%, respectively. It is apparent that the formation of the wetting liquid phase smoothens the strut surface by removing most surface pores. The surface roughness of the solid sintered filament and the liquid sintered filament has a Ra (arithmetic mean deviation) of 0.91 μm and 0.55 μm, respectively. Properties such as toughness [50], fatigue life [51], and corrosion resistance [52] are expected to benefit from the smoothened surface. From side-views of micro-lattices shown in Fig. 4(c), it is apparent that the Cu-rich phase is enriched at the joints connecting orthogonal filaments, forming nodes. The smoothing of the originally sharp cusps at the joints alleviates stress concentration during deformation and thus may lead to a higher ductility. The chemical compositions from EDS are $Co_{20.9}Cr_{17.7}Cu_{18.7}Fe_{22.1}Ni_{20.6}$ and $Co_{20.4}Cr_{18.1}Cu_{20.0}Fe_{21.4}Ni_{20.1}$ for solid sintered and liquid sintered samples, respectively, which are shown in the insert in Fig. 4(c). The compositions of Cu were tested by ICP, and no losses were found.

Annealing twins in Cu-poor grains are observed from the surface and inverse pole figures, which are probably formed to accommodate thermal expansion mismatch between phases and grains upon cooling. Similar annealing twins were reported in the CoCrFeNi alloy [24]. Inverse pole figures of solid-sintered and liquid-sintered samples are shown in Fig. 4(d). The Cu-rich and Cu-poor phases are not resolved by EBSD due to their similar lattice parameter and identical fcc crystal structure. There is no obvious texture for these sintered samples, as shown in Supplementary Figure 6. The grain sizes in solid-state and liquid-phase sintered specimens are 3 ± 1 and 11 ± 4 μm, respectively. The 10 min excursion to 1150 °C thus increases the grain size, as expected from the accelerated diffusion in the liquid Cu-rich phase. Rogal reported that grain growth caused by liquid phase in CoCrFeNiCu is limited because diffusion of Fe, Co, Ni ,and Cr in the Cu-rich liquid phase is slowed by the low solubility of these elements within liquid Cu [14]. It has been found that the addition of Cu in cast CoCrFeNi alloys reduces the grain size after comparing the microstructure of $CoCrFeNiCu_x$ (x=0, 0.2, 0.4, 0.6, 0.8, 1.0) alloys [13]. Previous research on a 3D ink-extrusion printed CoCrFeNi alloy showed a

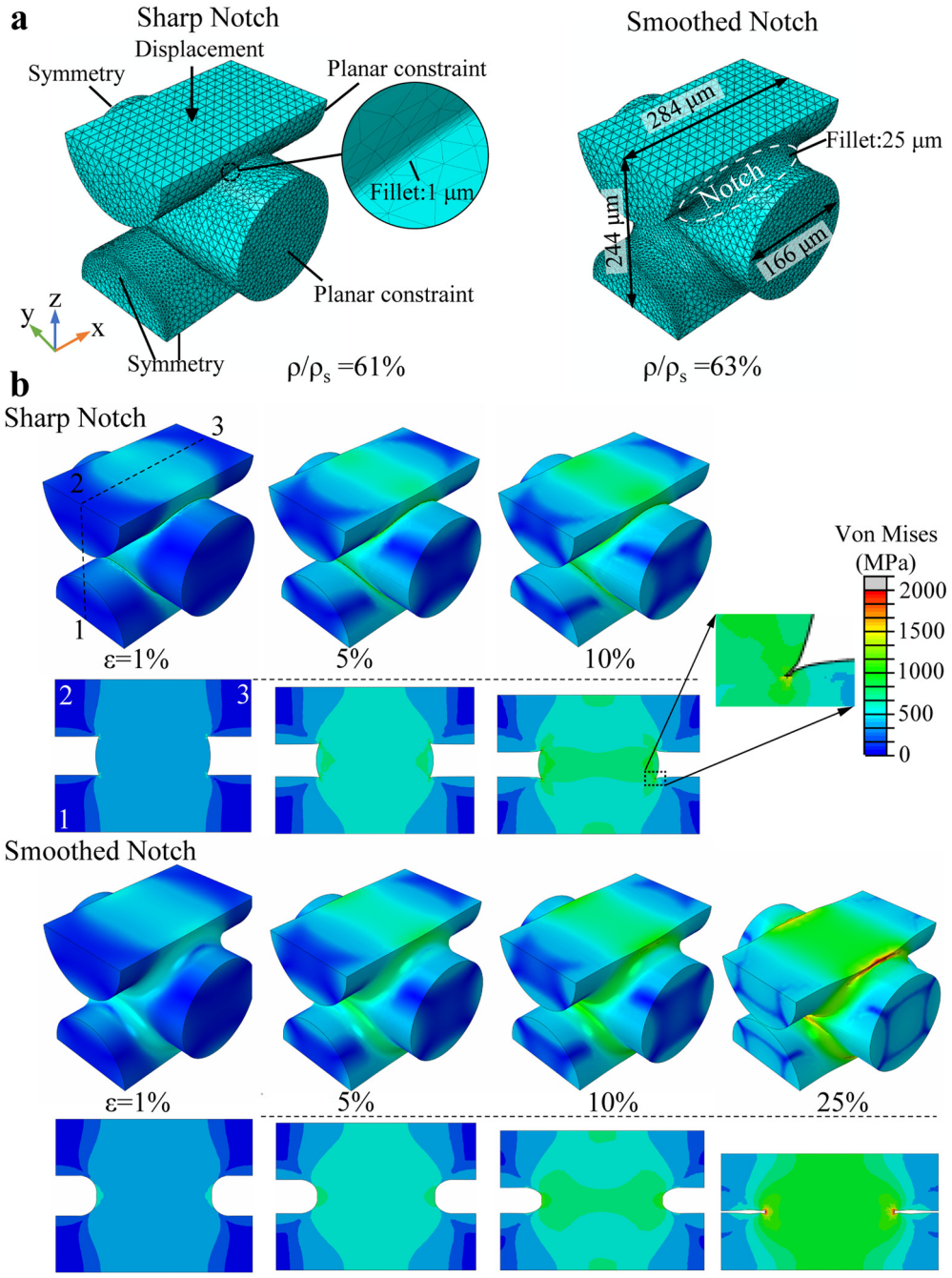

Fig. 6. FEM for two representative volume elements with different fillet radius (labeled Sharp Notch and Smoothed Notch) showing (a) meshing, boundary conditions, and dimensions, (b) von Mises stress distribution for uniaxial compressive strains ε = 1, 5, 10, and 25%

grain size of 35–80 μm within a filament, after sintering at 1300 °C for 1 h [24]. The addition of Cu in combination with liquid phase sintering at a much lower temperature of 1150 °C thus enables formation of near-fully dense material with a reduced grain size by a factor of 3-8, expected to increase strength. The hardness of solid-sintered and liquid-sintered CuCoCrFeNi are 1687 ± 69 MPa, and 1706 ± 78 MPa, respectively. The close hardness of these two samples indicates that the additional grain-boundary strengthening effect of the finer-grained solid-sintered sample may be masked by its residual porosity (1.6 ± 0.7%). In addition, Lin et al. [53,54] showed that Cu-rich precipitates within $CoCrFeNiCu_{0.5}$ do not contribute to a higher hardness after aging at 350-1350 °C for 24 h, likely due to the low strength of the Cu-rich phase.

3.3. Compressive Mechanical Properties

As shown in the compressive stress-strain curves of Fig. 5, liquid-sintered microlattices deform uniformly up to 47% compressive strain with a near-constant strain-hardening rate. The solid-sintered lattices, at comparable relative density ρ, show similar behavior, except with lower strain hardening at large strains, which is directly shown in Supplementary Figure 7 (b). As shown in Supplementary Figure 8, two solid-sintered lattices (ρ/ρ_s =60 and 68%) formed column-like or shear-like cracks on their surface which explain the stress drop observed at larger strains in Fig. 5. In contrast, no large-scale cracks are observed for liquid-sintered lattices, with a single, small crack observed on the sur-

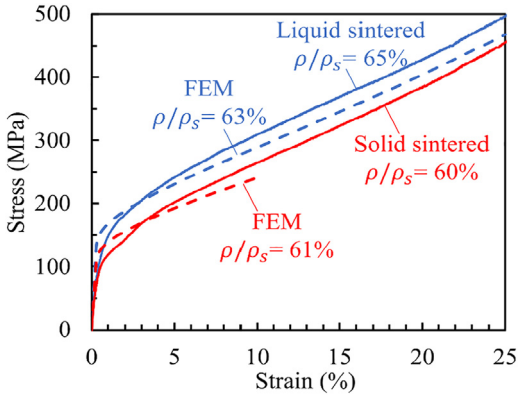

Fig. 7. Compressive stress-strain curves from FEM calculations (dotted lines) and experimental tests (solid lines) for microlattices for two different fillets (shown in Fig. 6) corresponding to solid and liquid-phase sintering. The FEM calculations for the solid-sintered lattice (with relative density ρ/ρ_s = 61%) are not carried out beyond 10% due to convergence difficulties stemming from self-contact.

face of a lattice with ρ/ρ_s=76% (Supplementary Figure 8). The superior compressive properties of liquid-sintered lattices, both in terms of ductility and load-bearing capability, are consistent with their smoother surfaces and joints, as well as their lower pore fraction within the struts, as compared to solid-sintered lattices. The deformed lattices with ρ/ρ_s=61% (liquid-sintered) and ρ/ρ_s=53% (solid-sintered) buckled, which explains their decreased hardening behavior after ~40% strain. The possible reason that can cause the buckling behavior of these lattices is that the lattices do not have perfect homogeneous lattice structures. For example, the cross-section of liquid sintered lattice shown in Supplementary Figure 5 (b) has denser regions on the right side because the printing head will deposit more materials at the turning position to print the next layer. The less-dense region will be deformed more easily and gradually leads to buckling of the lattice.

The compressive stress-strain curves of previously-studied Cu-free solid-sintered equiatomic CoCrFeNi lattices are also shown in Fig. 5. Our liquid-sintered CoCrFeNiCu lattices show a higher yield strength can be attributed to (i) the finer grains of CoCrFeNiCu, and (ii) the smoothened joints that alleviate stress concentration and delay yield. The reduced hardening behavior of our CoCrFeNiCu (especially at high strain) is possibly caused by the soft Cu-rich phase accommodating strain from the harder, Cu-poor phase. Also, our dual-phase CuCoCrFeNi alloy is expected to have higher toughness and damage-tolerance for the same reasons. For our liquid-sintered CoCuCrFeNi with higher stress sustained at a similar strain compared to CoCrFeNi, a higher energy absorption (i.e., the area under the stress-strain curve) is achieved.

3.4. Finite element modeling

To study the effect of smoothed notches on the mechanical behavior of 3D printed lattices, Abaqus CAD (2017) is used to perform finite-element modelling (FEM) of two 0/90° cross-ply lattices with 1 and 25 μm fillets at their nodes (Fig. 6a), representing lattices sintered in the solid and liquid states, respectively (Fig. 4(b)). Based on measurements of sintered lattices, a strut horizontal spacing of 284 μm, vertical spacing of 244 μm, and diameter of 166 μm are used in both representative volume elements (RVE). The relative densities of these models (the volume fraction occupied by solid struts) are 61 and 63% for solid- and liquid-sintered lattices, respectively. The RVE top surface is subjected to a uniform displacement in its normal direction. Two orthogonal side surfaces and the bottom surface of each RVE are subjected to symmetry conditions forbidding displacements in their normal direction. The other two adjacent side surfaces for each RVE have planar constraints, achieved using the "plane keeps plane" plugin in Abaqus to maintain these planes flat and perpendicular to the top and bottom surfaces after deformation. The boundary conditions and geometry parameters are shown in Fig. 6(a). These boundary conditions allow the lattice to develop Poisson's expansion during deformation while the four side faces are kept planar and perpendicular to top and bottom surfaces. Therefore, these representative volume elements (RVE) are directly representative of a very large lattice, by using translation symmetry before and after deformation.

The input properties for the CoCrCuFeNi HEA include solid density ρ_s = 8.33 g/cm^3 calculated from elemental densities, Poisson's ratio ν = 0.28 [55] from CoCrFeNi, and Young's modulus E = 155.1 GPa (calculated as E=3K(1-2ν), where the bulk modulus K is 117.5 GPa [56]). As shown in Supplementary Figure 9, the input for plastic deformation (a compressive stress-strain curve) is taken from Ref. [14] for a thixo-formed (1150 °C) CoCrCuFeNi HEA with a similar microstructure to our liquid-sintered lattice.

Fig. 6(b) shows the distribution of von Mises stress within the RVE after 1, 5, 10, and 25% uniaxial compressive strain. As shown in the cross-section labeled "1-2-3", the smoothened notch reduces the level of stress concentration. The stress-strain curves calculated from FEM are shown in Fig. 7, which confirms that the sample with the smoothened notch exhibits a higher yield strength. A good match is found with the experimental measurements of the lattices. As the uniaxial strain increases from 1 to 5 and to 10%, the stress distributions within the two RVEs converge (Fig. 6(b)), which explains the similar hardening behavior in the stress-strain curves (Fig. 7). As shown in Supplementary Figure 10, tensile principal stresses (σ_{xx}) from the Poisson's effect are found in horizontal struts, more so for lattices with sharp than smoothed notches. Because of their tensile nature, these can lead to crack initiation and growth, consistent with the observation that solid-sintered lattices are less ductile than liquid-sintered lattices.

Several factors that may potentially contribute to deviations between FEM predictions and experimental results should be noted. Our FEM model does not capture the barreling effect caused by friction between the sample and contacting plates that can contribute to a higher strength. The input for compression property in FEM (Supplementary Figure 9) comes from semi-solid cast CoCrCuFeNi, which has neither exactly the same composition nor exactly the same microstructure as our samples. In addition, a perfect lattice macro-structure consisting of many representative volume elements (RVE) shown in Fig. 6 is used to simplify the actual lattice macro-structure (Supplementary Figure 5). However, our FEM analysis clearly shows that smoothed notches achieved by liquid sintering can effectively alleviate the stress concentration and delay the onset of yield and that the formation of a wetting liquid during post-heat treatment is desirable.

4. Conclusions

In this study, in-situ diffraction is used to study the co-reduction of a blend of Co_3O_4, CuO, Fe_2O_3, NiO, and Cr_2O_3 oxide powders and the following interdiffusion of the five reduced metallic elements, Co, Cr, Cu, Fe, and Ni. An ink containing a powder blend of oxides (Co_3O_4, CuO, Fe_2O_3, NiO) and metallic Cr is used to fabricate lattices by 3D-ink extrusion printing which are subsequently reduced with H_2 to the equiatomic HEA CoCrCuFeNi composition. The phase and microstructural evolution during reduction and sintering, and the mechanical properties of lattices are investigated. The main conclusions are:

(1) A blend of binary oxide powders - Co_3O_4, CuO, Fe_2O_3, NiO, and Cr_2O_3 - was reduced under hydrogen by heating from 20 to 943°C. The first four oxides start reduction in a narrow temperature range of 285-319 °C, which is completed

at 315-377 °C, forming metallic Co, Cu, Fe, and Ni. Cr_2O_3 is gradually reduced to Cr between 824 and 943 °C, and remains partially unreduced at 943 °C, due to its high stability. Upon interdiffusion of the nascent metals, a Cu-poor and a Cu-rich phase are formed.

(2) Using metallic Cr rather than Cr_2O_3 in the above blend, a nearly fully reduced, dense, and homogenous two-phase alloy is achieved when solid-state sintered at 1050 or 1100 °C for 4 h, below the solidus temperature of 1112 °C. Liquid-phase sintering - achieved via a 10 min excursion at 1150 °C - produces a Cu-rich melt which wets the solid Cu-poor phase and removes residual pores effectively.

(3) The liquid-sintered microlattices, because of the formation of the Cu-rich melt, exhibit smoothed cusps between struts, unlike the sharp cusps in the solid-sintered microlattices. This reduction of stress concentration is predicted, via finite-element modeling, to lead to higher strength and ductility, in agreement with experimental compressive tests.

Data availability

The data that support the findings of this study are available from the corresponding author upon reasonable request.

Competing interest

DCD discloses a financial interest in Metalprinting, Inc. (South Korea) which is active in ink-based materials printing.

Declaration of competing interest

The authors declare that they have no known competing financial interests or personal relationships that could have appeared to influence the work reported in this paper.

Acknowledgement

This research received funding from the National Science Foundation (NSF DMR-2004769). CK received partial funding from the Swiss National Science Foundation as an Early Postdoc Mobility fellowship under grant No. 172180. We gratefully acknowledge the Paul Scherrer Institut, Villigen, Switzerland and Dr. N. Casati for the provision of beam-time for diffraction experiments at the Material Science beamline of the Swiss Light Source; and M. Lange for technical support at the beamline. This research made use of Northwestern University's MatSCI and CLaMMP facilities that received support from the MRSEC program (NSF DMR-1720139) of the Materials Research Center, EPIC facilities at NUANCE center that received support from Soft and Hybrid Nanotechnology Experimental (SHyNE) Resource (NSF ECCS-1542205), the International Institute for Nanotechnology (IIN), the MRSEC program (NSF DMR-1720139) at the Materials Research Center, the Keck Foundation, and the State of Illinois, through the IIN. We thank Prof. Samuel Stupp (NU) for use of his Bioplotter for ink printing, and Prof. Jian Cao (NU) for use of her workstation for modeling work.

Supplementary materials

Supplementary material associated with this article can be found, in the online version, at doi:10.1016/j.actamat.2022.118187.

References

[1] J.-W. Yeh, S.-K. Chen, S.-J. Lin, J.-Y. Gan, T.-S. Chin, T.-T. Shun, C.-H. Tsau, S.-Y. Chang, Nanostructured High-Entropy Alloys with Multiple Principal Elements: Novel Alloy Design Concepts and Outcomes, Adv. Eng. Mater. 6 (5) (2004) 299–303.
[2] B. Cantor, I.T.H. Chang, P. Knight, A.J.B. Vincent, Microstructural development in equiatomic multicomponent alloys, Mater. Sci. Eng., A 375-377 (2004) 213–218.
[3] N. Ma, S. Liu, W. Liu, L. Xie, D. Wei, L. Wang, L. Li, B. Zhao, Y. Wang, Research Progress of Titanium-Based High Entropy Alloy: Methods, Properties, and Applications, Frontiers in Bioengineering and Biotechnology 8 (2020).
[4] E.P. George, W.A. Curtin, C.C. Tasan, High entropy alloys: A focused review of mechanical properties and deformation mechanisms, Acta Mater 188 (2020) 435–474.
[5] D.H. Xiao, P.F. Zhou, W.Q. Wu, H.Y. Diao, M.C. Gao, M. Song, P.K. Liaw, Microstructure, mechanical and corrosion behaviors of AlCoCuFeNi-(Cr,Ti) high entropy alloys, Mater. Des. 116 (2017) 438–447.
[6] C. Du, L. Hu, Q. Pan, K. Chen, P. Zhou, G. Wang, Effect of Cu on the strengthening and embrittling of an FeCoNiCr-xCu HEA, Mater. Sci. Eng., A 832 (2022) 142413.
[7] B. Wu, Z. Xie, J. Huang, J. Lin, Y. Yang, L. Jiang, J. Huang, G. Ye, C. Zhao, S. Yang, B. Sa, Microstructures and thermodynamic properties of high-entropy alloys CoCrCuFeNi, Intermetallics 93 (2018) 40–46.
[8] S. Nam, J.Y. Hwang, J. Jeon, J. Park, D. Bae, M.J. Kim, J.-H. Kim, H. Choi, Deformation behavior of nanocrystalline and ultrafine-grained CoCrCuFeNi high-entropy alloys, J. Mater. Res. 34 (5) (2019) 720–731.
[9] N. Park, I. Watanabe, D. Terada, Y. Yokoyama, P.K. Liaw, N. Tsuji, Recrystallization Behavior of CoCrCuFeNi High-Entropy Alloy, Metall. Mater. Trans. A 46 (4) (2015) 1481–1487.
[10] E. Zhou, D. Qiao, Y. Yang, D. Xu, Y. Lu, J. Wang, J.A. Smith, H. Li, H. Zhao, P.K. Liaw, F. Wang, A novel Cu-bearing high-entropy alloy with significant antibacterial behavior against corrosive marine biofilms, Journal of Materials Science & Technology 46 (2020) 201–210.
[11] J. Gao, Y. Jin, Y. Fan, D. Xu, L. Meng, C. Wang, Y. Yu, D. Zhang, F. Wang, Fabricating antibacterial CoCrCuFeNi high-entropy alloy via selective laser melting and in-situ alloying, Journal of Materials Science & Technology 102 (2022) 159–165.
[12] Z. Li, D. Qiao, Y. Xu, E. Zhou, C. Yang, X. Yuan, Y. Lu, J.-D. Gu, S. Wolfgang, D. Xu, Cu-bearing high-entropy alloys with excellent antiviral properties, Journal of Materials Science & Technology (2021).
[13] A. Verma, P. Tarate, A.C. Abhyankar, M.R. Mohape, D.S. Gowtam, V.P. Deshmukh, T. Shanmugasundaram, High temperature wear in CoCrFeNiCux high entropy alloys: The role of Cu, Scripta Mater 161 (2019) 28–31.
[14] Ł. Rogal, Semi-solid processing of the CoCrCuFeNi high entropy alloy, Mater. Des. 119 (2017) 406–416.
[15] D. Herzog, V. Seyda, E. Wycisk, C. Emmelmann, Additive manufacturing of metals, Acta Mater 117 (2016) 371–392.
[16] A. Ostovari Moghaddam, N.A. Shaburova, M.N. Samodurova, A. Abdollahzadeh, E.A. Trofimov, Additive manufacturing of high entropy alloys: A practical review, Journal of Materials Science & Technology 77 (2021) 131–162.
[17] Z. Qiu, C. Yao, K. Feng, Z. Li, P.K. Chu, Cryogenic deformation mechanism of CrMnFeCoNi high-entropy alloy fabricated by laser additive manufacturing process, International Journal of Lightweight Materials and Manufacture 1 (1) (2018) 33–39.
[18] T. Fujieda, H. Shiratori, K. Kuwabara, T. Kato, K. Yamanaka, Y. Koizumi, A. Chiba, First demonstration of promising selective electron beam melting method for utilizing high-entropy alloys as engineering materials, Mater. Lett. 159 (2015) 12–15.
[19] P. Agrawal, S. Thapliyal, S.S. Nene, R.S. Mishra, B.A. McWilliams, K.C. Cho, Excellent strength-ductility synergy in metastable high entropy alloy by laser powder bed additive manufacturing, Addit. Manuf. 32 (2020) 101098.
[20] S. Xiang, H. Luan, J. Wu, K.-F. Yao, J. Li, X. Liu, Y. Tian, W. Mao, H. Bai, G. Le, Q. Li, Microstructures and mechanical properties of CrMnFeCoNi high entropy alloys fabricated using laser metal deposition technique, J. Alloys Compd. 773 (2019) 387–392.
[21] R.J. Vikram, B.S. Murty, D. Fabijanic, S. Suwas, Insights into micro-mechanical response and texture of the additively manufactured eutectic high entropy alloy AlCoCrFeNi2.1, J. Alloys Compd. 827 (2020) 154034.
[22] Z.-C. Fang, Z.-L. Wu, C.-G. Huang, C.-W. Wu, Review on residual stress in selective laser melting additive manufacturing of alloy parts, Optics & Laser Technology 129 (2020) 106283.
[23] A.E. Jakus, S.L. Taylor, N.R. Geisendorfer, D.C. Dunand, R.N. Shah, Metallic Architectures from 3D-Printed Powder-Based Liquid Inks, Adv. Funct. Mater. 25 (45) (2015) 6985–6995.
[24] C. Kenel, N.P. Casati, D.C. Dunand, 3D ink-extrusion additive manufacturing of CoCrFeNi high-entropy alloy micro-lattices, Nature communications 10 (1) (2019) 1–8.
[25] S.L. Taylor, R.N. Shah, D.C. Dunand, Ni-Mn-Ga micro-trusses via sintering of 3D-printed inks containing elemental powders, Acta Mater 143 (2018) 20–29.
[26] S.L. Taylor, A.E. Jakus, R.N. Shah, D.C. Dunand, Iron and Nickel Cellular Structures by Sintering of 3D-Printed Oxide or Metallic Particle Inks, Adv. Eng. Mater 19 (11) (2017) 1600365.
[27] S.L. Taylor, A.J. Ibeh, A.E. Jakus, R.N. Shah, D.C. Dunand, NiTi-Nb micro-trusses fabricated via extrusion-based 3D-printing of powders and transient-liquid-phase sintering, Acta Biomaterialia 76 (2018) 359–370.
[28] M. Calvo, A.E. Jakus, R.N. Shah, R. Spolenak, D.C. Dunand, Microstructure and Processing of 3D Printed Tungsten Microlattices and Infiltrated W–Cu Composites, Adv. Eng. Mater 20 (9) (2018) 1800354.
[29] B. Song, C. Kenel, D.C. Dunand, 3D ink-extrusion printing and sintering of Ti, Ti-TiB and Ti-TiC microlattices, Addit. Manuf. 35 (2020) 101412.

[30] S. Eqtesadi, A. Motealleh, F.H. Perera, P. Miranda, A. Pajares, R. Wendelbo, F. Guiberteau, A.L. Ortiz, Fabricating geometrically-complex B4C ceramic components by robocasting and pressureless spark plasma sintering, Scripta Mater 145 (2018) 14–18.
[31] X. Wang, Y. Sun, C. Peng, H. Luo, R. Wang, D. Zhang, Transitional Suspensions Containing Thermosensitive Dispersant for Three-Dimensional Printing, ACS Appl. Mater. Interfaces 7 (47) (2015) 26131–26136.
[32] D. Zhang, C. Kenel, D.C. Dunand, Microstructure and properties of additively-manufactured WC-Co microlattices and WC-Cu composites, Acta Mater 221 (2021) 117420.
[33] D. Zhang, C. Kenel, M. Caccia, K.H. Sandhage, D.C. Dunand, Complex-shaped, finely-featured ZrC/W composites via shape-preserving reactive melt infiltration of porous WC structures fabricated by 3D ink extrusion, Additive Manufacturing Letters 1 (2021) 100018.
[34] C. Meier, R. Weissbach, J. Weinberg, W.A. Wall, A.J. Hart, Critical influences of particle size and adhesion on the powder layer uniformity in metal additive manufacturing, J. Mater. Process. Technol. 266 (2019) 484–501.
[35] P. Kiani, U. Scipioni Bertoli, A.D. Dupuy, K. Ma, J.M. Schoenung, A Statistical Analysis of Powder Flowability in Metal Additive Manufacturing, Adv. Eng. Mater. 22 (10) (2020) 2000022.
[36] S. Peng, S. Mooraj, R. Feng, L. Liu, J. Ren, Y. Liu, F. Kong, Z. Xiao, C. Zhu, P.K. Liaw, W. Chen, Additive manufacturing of three-dimensional (3D)-architected CoCrFeNiMn high- entropy alloy with great energy absorption, Scripta Mater 190 (2021) 46–51.
[37] K.M. Thyng, C.A. Greene, R.D. Hetland, H.M. Zimmerle, S.F. DiMarco, True colors of oceanography: Guidelines for effective and accurate colormap selection, Oceanography 29 (3) (2016) 9–13.
[38] P.H. Eilers, H.F. Boelens, Baseline correction with asymmetric least squares smoothing, Leiden University Medical Centre Report 1 (1) (2005) 5.
[39] J.H. Nadler, T.H. Sanders, R.F. Speyer, Oxide reduction and sintering of Fe–Cr alloy honeycombs, J. Mater. Res. 18 (8) (2003) 1787–1794.
[40] T.H.S. Jr. J.H. Nadler, J.K. Cochran, S.S. Kim, Oxide reduction and diffusion in Fe-Cr alloy honeycombs, J. Phys. IV France 120 (2004) 47–54.
[41] M.A. Turchanin, P.G. Agraval, Phase equilibria and thermodynamics of binary copper systems with 3d-metals. V. Copper-cobalt system, Powder Metall. Met. Ceram. 46 (1) (2007) 77–89.
[42] R.P. Shi, C.P. Wang, D. Wheeler, X.J. Liu, Y. Wang, Formation mechanisms of self-organized core/shell and core/shell/corona microstructures in liquid droplets of immiscible alloys, Acta Mater 61 (4) (2013) 1229–1243.
[43] M.A. Turchanin, Phase equilibria and thermodynamics of binary copper systems with 3d-metals. III. Copper-chromium system, Powder Metall. Met. Ceram. 45 (9) (2006) 457–467.
[44] J. Sopousek, J. Vrestal, J. Pinkas, P. Broz, J. Bursik, A. Styskalik, D. Skoda, O. Zobac, J. Lee, Cu–Ni nanoalloy phase diagram – Prediction and experiment, Calphad 45 (2014) 33–39.
[45] S. Thangaraju, E. Bouzy, A. Hazotte, Phase Stability of a Mechanically Alloyed CoCrCuFeNi High Entropy Alloy, Adv. Eng. Mater 19 (8) (2017) 1700095.
[46] J.-M. Zhu, J.-L. Meng, J.-L. Liang, Microstructure and mechanical properties of multi-principal component AlCoCrFeNiCuxalloy, Rare Metals 35 (5) (2016) 385–389.
[47] H. Zheng, R. Chen, G. Qin, X. Li, Y. Su, H. Ding, J. Guo, H. Fu, Microstructure evolution, Cu segregation and tensile properties of CoCrFeNiCu high entropy alloy during directional solidification, Journal of Materials Science & Technology 38 (2020) 19–27.
[48] S. Bagehorn, J. Wehr, H.J. Maier, Application of mechanical surface finishing processes for roughness reduction and fatigue improvement of additively manufactured Ti-6Al-4V parts, Int. J. Fatigue 102 (2017) 135–142.
[49] E. Maleki, S. Bagherifard, M. Bandini, M. Guagliano, Surface post-treatments for metal additive manufacturing: Progress, challenges, and opportunities, Addit. Manuf. 37 (2021) 101619.
[50] C. de Formanoir, S. Michotte, O. Rigo, L. Germain, S. Godet, Electron beam melted Ti–6Al–4V: Microstructure, texture and mechanical behavior of the as-built and heat-treated material, Mater. Sci. Eng., A 652 (2016) 105–119.
[51] T. Persenot, A. Burr, R. Dendievel, J.-Y. Buffière, E. Maire, J. Lachambre, G. Martin, Fatigue performances of chemically etched thin struts built by selective electron beam melting: Experiments and predictions, Materialia 9 (2020) 100589.
[52] C. Ma, M.T. Andani, H. Qin, N.S. Moghaddam, H. Ibrahim, A. Jahadakbar, A. Amerinatanzi, Z. Ren, H. Zhang, G.L. Doll, Y. Dong, M. Elahinia, C. Ye, Improving surface finish and wear resistance of additive manufactured nickel-titanium by ultrasonic nano-crystal surface modification, J. Mater. Process. Technol. 249 (2017) 433–440.
[53] C.-M. Lin, H.-L. Tsai, H.-Y. Bor, Effect of aging treatment on microstructure and properties of high-entropy Cu0.5CoCrFeNi alloy, Intermetallics 18 (6) (2010) 1244–1250.
[54] C.-M. Lin, H.-L. Tsai, Equilibrium phase of high-entropy FeCoNiCrCu0.5 alloy at elevated temperature, J. Alloys Compd. 489 (1) (2010) 30–35.
[55] Z. Wu, H. Bei, G.M. Pharr, E.P. George, Temperature dependence of the mechanical properties of equiatomic solid solution alloys with face-centered cubic crystal structures, Acta Mater 81 (2014) 428–441.
[56] P.F. Yu, L.J. Zhang, H. Cheng, H. Zhang, M.Z. Ma, Y.C. Li, G. Li, P.K. Liaw, R.P. Liu, The high-entropy alloys with high hardness and soft magnetic property prepared by mechanical alloying and high-pressure sintering, Intermetallics 70 (2016) 82–87.